# *Aerosol and cloud microphysics covariability in the northeast Pacific boundary layer estimated with ship-based and satellite remote sensing observations*

Article

Published Version

Painemal, D., Chiu, J.-Y. C., Minnis, P., Yost, C., Zhou, X., Cadeddu, M., Eloranta, E., Lewis, E. R., Ferrare, R. and Kollias, P. (2017) Aerosol and cloud microphysics covariability in the northeast Pacific boundary layer estimated with ship-based and satellite remote sensing observations. Journal of Geophysical Research: Atmospheres, 122 (4). pp. 2403-2418. ISSN 2169-8996 doi: https://doi.org/10.1002/2016JD025771 Available at https://centaur.reading.ac.uk/69505/



To link to this article DOI: http://dx.doi.org/10.1002/2016JD025771

Publisher: American Geophysical Union

AGU PUBLICATIONS

JGR

Journal of Geophysical Research: Atmospheres

RESEARCH ARTICLE

10.1002/2016JD025771

**Key Points:**

- Satellite and ship-based remote sensing cloud retrievals are used to calculate the aerosol-cloud covariability in the NE Pacific
- CCN, accumulation mode aerosol, and extinction coefficient yield consistently high covariability, near the physical upper limit
- Computed aerosol-cloud interaction is consistent with aircraft studies in the eastern Pacific, especially for well-mixed boundary layers

**Correspondence to:**
D. Painemal,
david.painemal@nasa.gov

**Citation:**
Painemal, D., J.-Y. C. Chiu, P. Minnis, C. Yost, X. Zhou, M. Cadeddu, E. Eloranta, E. R. Lewis, R. Ferrare, and P. Kollias (2017), Aerosol and cloud microphysics covariability in the northeast Pacific boundary layer estimated with ship-based and satellite remote sensing observations, *J. Geophys. Res. Atmos.*, *122*, doi:10.1002/2016JD025771.

Received 10 AUG 2016
Accepted 13 FEB 2017
Accepted article online 14 FEB 2017



# Aerosol and cloud microphysics covariability in the northeast Pacific boundary layer estimated with ship-based and satellite remote sensing observations

**David Painemal[1,2], J.-Y. Christine Chiu[3], Patrick Minnis[2], Christopher Yost[1], Xiaoli Zhou[4], Maria Cadeddu[5], Edwin Eloranta[6], Ernie R. Lewis[7], Richard Ferrare[2], and Pavlos Kollias[8]**

[1]Science Systems and Applications, Inc., Hampton, Virginia, USA, [2]NASA Langley Research Center, Hampton, Virginia, USA, [3]Department of Meteorology, University of Reading, Reading, UK, [4]Department of Atmospheric and Oceanic Sciences, McGill University, Montreal, Quebec, Canada, [5]Environmental Science Division, Argonne National Laboratory, Lemont, Illinois, USA, [6]Space Science and Engineering Center, University of Wisconsin-Madison, Madison, Wisconsin, USA, [7]Brookhaven National Laboratory, Upton, New York, USA, [8]School of Marine and Atmospheric Sciences, Stony Brook University, Stony Brook, New York, USA

**Abstract** Ship measurements collected over the northeast Pacific along transects between the port of Los Angeles (33.7°N, 118.2°W) and Honolulu (21.3°N, 157.8°W) during May to August 2013 were utilized to investigate the covariability between marine low cloud microphysical and aerosol properties. Ship-based retrievals of cloud optical depth ($\tau$) from a Sun photometer and liquid water path (LWP) from a microwave radiometer were combined to derive cloud droplet number concentration $N_d$ and compute a cloud-aerosol interaction (ACI) metric defined as $\mathrm{ACI_{CCN}} = \partial \ln(N_d)/\partial \ln(\mathrm{CCN})$, with CCN denoting the cloud condensation nuclei concentration measured at 0.4% ($\mathrm{CCN_{0.4}}$) and 0.3% ($\mathrm{CCN_{0.3}}$) supersaturation. Analysis of $\mathrm{CCN_{0.4}}$, accumulation mode aerosol concentration ($N_a$), and extinction coefficient ($\sigma_{\mathrm{ext}}$) indicates that $N_a$ and $\sigma_{\mathrm{ext}}$ can be used as $\mathrm{CCN_{0.4}}$ proxies for estimating ACI. $\mathrm{ACI_{CCN}}$ derived from 10 min averaged $N_d$ and $\mathrm{CCN_{0.4}}$ and $\mathrm{CCN_{0.3}}$, and $\mathrm{CCN_{0.4}}$ regressions using $N_a$ and $\sigma_{\mathrm{ext}}$, produce high $\mathrm{ACI_{CCN}}$: near 1.0, that is, a fractional change in aerosols is associated with an equivalent fractional change in $N_d$. $\mathrm{ACI_{CCN}}$ computed in deep boundary layers was small ($\mathrm{ACI_{CCN}} = 0.60$), indicating that surface aerosol measurements inadequately represent the aerosol variability below clouds. Satellite cloud retrievals from MODerate-resolution Imaging Spectroradiometer and GOES-15 data were compared against ship-based retrievals and further analyzed to compute a satellite-based $\mathrm{ACI_{CCN}}$. Satellite data correlated well with their ship-based counterparts with linear correlation coefficients equal to or greater than 0.78. Combined satellite $N_d$ and ship-based $\mathrm{CCN_{0.4}}$ and $\mathrm{N_a}$ yielded a maximum $\mathrm{ACI_{CCN}} = 0.88$–$0.92$, a value slightly less than the ship-based $\mathrm{ACI_{CCN}}$, but still consistent with aircraft-based studies in the eastern Pacific.

## 1. Introduction

The aerosol indirect effect (AIE) in low marine clouds remains a central source of uncertainty in climate models, hampering our ability to accurately quantify anthropogenic radiative forcing [e.g., *Rosenfeld et al.*, 2014; *Carslaw et al.*, 2013, and references therein]. Reduction of AIE intermodel spread thus requires accurate measurements of cloud and aerosol properties that can guide future improvements in model parameterizations. However, the use of AIE estimates from observations is challenging because different platforms can yield a broad range of AIE values [e.g., *McComiskey and Feingold*, 2008]. While this variability can be partially due to the unique atmospheric characteristics of the cloud regimes sampled (e.g., maritime versus continental), less attention has been paid to the physical representativeness of the observations. In fact, even when the measurements are accurate within some tolerable errors, different aerosol measurements might not yield the same covariability with the cloud microphysics. Since the property that is most directly linked to cloud droplet formation is ultimately cloud condensation nuclei (CCN) concentration, the suitability of other aerosol measurements depends on how well they can reproduce CCN concentration variability. For instance, *Shinozuka et al.* [2015] show a close correlation between CCN concentration and aerosol extinction coefficient over the oceans, with fractional changes in extinction yielding smaller fractional changes in CCN concentration. Similarly, attempts have been made to use aerosol optical depth (AOD) as a proxy for CCN concentration [e.g., *Andreae*, 2009]. Although CCN concentration and AOD correlate well when considering a broad range of aerosol concentrations, the relationship is poorly characterized in pristine maritime environments [e.g., *Andreae*, 2009, Figure 1], likely because of a few large aerosol particles that contribute little to CCN concentration but dominate the AOD. This is particularly troublesome as it is common to use satellite-based AOD for evaluating AIE model performance [e.g., *Quaas et al*., 2009]. Interestingly, *Painemal and Zuidema* [2010] and *Painemal et al*. [2015] show that the combined use of satellite cloud microphysics and in situ CCN concentration can produce robust correlations in cloud-topped marine boundary layers. Nevertheless, consistency between ground-based and satellite-based remote sensing estimates of AIE has not been investigated with the necessary detail.

For better observational quantification of AIE, it would be desirable to adopt a regional focus and rely on the redundancy and consistency of both instruments and retrievals. By adopting a regional focus, one can better isolate the meteorological processes and aerosol chemical properties that dictate changes in the aerosol-cloud covariability. Redundancy, on the other hand, will help determine the robustness of the observations and help evaluate the advantages of different aerosol and cloud proxies. Although these requirements are met by the multiobservational platforms deployed by the Atmospheric Radiation Measurement (ARM) program [e.g., *Miller et al*., 2016], long-term observations over marine environments have been elusive until a recent ARM field campaign over the northeast Pacific: the Marine ARM GPCI (Global Energy and Water Cycle Experiment (GEWEX) Cloud System Study (GCSS) Pacific cross-section intercomparison) Investigation of Clouds (MAGIC) campaign [*Lewis and Teixeira*, 2015; *Zhou et al*., 2015]. MAGIC deployed the second ARM mobile facility (AMF2) on board a cargo ship, the Horizon *Spirit*, that sailed between the ports of Los Angeles, California (33.7°N, 118.2°W) and Honolulu, Hawaii (21.3°N, 157.8°W) during two observation periods: September (2012)–January (2013) and May–September of 2013. AMF2 included a suite of aerosol probes that measured surface CCN concentration, aerosol size distribution, and aerosol light scattering; radiometric instrumentation for cloud retrievals; a high spectral resolution lidar (HSRL); and Ka band and W band radars [e.g., *Kollias et al*., 2016].

This work builds on a recent article [*Painemal et al*., 2015, hereinafter P15] that describes seasonal changes and synoptic patterns that influence aerosol and cloud microphysics variability during MAGIC. Here we follow a more specific focus by centering our efforts on quantifying the covariability and the cloud-aerosol interaction metric $ACI_\alpha = \partial \ln(N_d)/\partial \ln(\alpha))$ between different aerosols properties ($\alpha$) and cloud droplet number concentration ($N_d$) by utilizing MAGIC in situ and remote sensors as well as satellite observations during Spring-Summer of 2013.

## 2. Data Set

We make extensive use of numerous MAGIC observations, which encompass standard meteorological observations and radiosondes, along with specific instrumentation unique to this deployment, which included passive and active remote sensors. We also complemented the ship data with retrievals from two satellite sensors, the Fifteenth Geostationary Operational Environmental Satellite (GOES-15) imager and the MODerate-resolution Imaging Spectroradiometer (MODIS) on the Terra and Aqua satellites. The data sets are described below and summarized in Table 1.

### 2.1. Ship-Based Aerosol Observations:

Cloud condensation nuclei concentrations were measured with a CCN counter [*Roberts and Nenes*, 2005] manufactured by Droplet Measurements Technology (DMT). The CCN counter varies supersaturations from 0% to 0.6% every 10 min. CCN concentrations at 0.4% were primarily used in this study, with additional analyses of 0.3% and 0.2% supersaturation CCN. These supersaturation values are consistent with the 0.3% used by *Hegg et al*. [2012], based on aircraft observations in California coastal stratocumulus clouds reported by *Hudson et al*. [2010]. Dry aerosol size distributions were measured with the DMT Ultrahigh Sensitivity Aerosol Spectrometer (UHSAS), which is a laser-based optical scattering, aerosol particle spectrometer that sizes aerosol particles with optical diameter between 60 and 1000 nm in 100 equally spaced logarithmic bins by the amount of light they scatter into given angular regions from a 1054 nm laser [*Cai et al*., 2008]. Aerosol light scattering was measured at three wavelengths: 450, 550, and 750 nm, with a TSI Integrating Nephelometer model 3563 [*Anderson et al*., 1996] that alternately sampled particles with aerodynamic diameters less than 1 and 10 μm. Aerosol light absorption was measured by a particle soot absorption photometer (PSAP, manufactured by Radiance Research, Inc.) at 470, 522, and 660 nm based on optical

**Table 1.** Instruments and Associated Measurements/Retrievals

| Instrument | Measurements/Retrievals |
|---|---|
| CCN particle counter | CCN concentrations at different supersaturations from 0 to 0.6% |
| Cimel Sun photometer | Cloud optical depth ($\tau$), effective radius ($r_e$), liquid water path (LWP), and cloud droplet number concentration ($N_d$, equation (2)) |
| Ultrahigh sensitivity aerosol spectrometer (UHSAS) | Aerosol size distribution, accumulation mode dry aerosol concentration ($N_a$, diameters between 0.1 and 1.0 μm) |
| Nephelometer | Aerosol scattering coefficient at wavelengths 450, 550, and 700 nm; instrument alternates measurements for particles with aerodynamic diameters less than 1 μm and less than 10 μm. |
| Particle soot absorption photometer (PSAP) | Aerosol absorption coefficient ($\sigma_{abs}$) at wavelengths 470, 522, and 660 nm; instrument alternates measurements for particles with aerodynamic diameters less than 1 μm and less than 10 μm. |
| Three-channel microwave radiometer | Liquid water path and $N_d$ (equation (2)) |
| K band radar | Cloud layers detection, cloud top height, and precipitation flag |
| University of Wisconsin's high spectral resolution lidar (HSRL) | Cloud base height detection and aerosol backscatter cross section ($\sigma_{back}$) |
| Ceilometer | Cloud base height detection and cloud frequency of occurrence |
| GOES-15 satellite imager | Daytime $r_e$ and $\tau$; $N_d$ derived from equation (3) |
| MODIS (Aqua and Terra satellites) | Daytime $r_e$ and $\tau$; $N_d$ derived from equation (3) |

transmittance measurements through a glass/cellulose filter over time as particles are deposited. The data, obtained for aerodynamic diameters less than 1 and 10 μm, are corrected for scattering and filter loading as described in *Bond et al*. [1999]. We adjusted the PSAP absorption to the nephelometer wavelength of 550 nm using the Ångström exponent determined from measurements at 470 and 660 nm, that is, assuming linearity between the logarithm of the absorption coefficient and logarithm of the wavelength. The University of Wisconsin High Spectral Resolution Lidar (HSRL) [*Eloranta*, 2005] provided information about the vertical distribution of aerosols and cloud boundary detection. The instrument operates at a 532 nm wavelength, with a field of view of 100 μrad and a range resolution of 7.5 m. Here we utilize the particle backscatter cross section because it is a robust retrieval and not strongly affected by calibration issues and signal noise.

### 2.2. Ship-Based Cloud Observations

Liquid water path was retrieved from a three-channel microwave radiometer (MWR), with a 3° field of view and three channels at 23.83, 30, and 89 GHz, with the last providing further constraint that enables retrieving more accurate LWP for thin clouds. These retrievals, based on iterative radiative calculations under an optimal estimation framework [*Cadeddu et al*., 2013], have been recently used for evaluating satellite microwave liquid water and water vapor paths [*Painemal et al*., 2016]. The effect of the ship motion was accounted for in the instrument calibration. Moreover, given the instrument's relatively large field of view, and typical angular departures from zenith were less than 1° [*Chiu et al*., 2016], the ship motion effects in the MWR measurements are deemed small.

Cloud base height was determined from a Vaisala CL31 laser ceilometer and the HSRL with vertical resolution of 7.5 m, using for the latter a particle backscatter cross-section threshold of $1 \cdot 10^{-4} \mathrm{m}^{-1} \mathrm{sr}^{-1}$, as in *Fielding et al*. [2015]. Cloud frequency was defined from the ceilometer as the ratio of the number of cloudy samples to the total. Cloud top height and precipitation detection were derived from a K band radar as in *Zhou et al*. [2015] using a hydrometeor mask algorithm based on the methodology by *Hildebrand and Sekhon* [1974] for the determination of noise level. The K band radar's high temporal resolution of 0.4 s oversampled the ship motion, allowing compensation of the motion effect by averaging the radar data to 4 s [*Zhou et al*., 2015]. A precipitation event is defined for times when an echo was detected in the lowest radar gate (~150 m). This definition encompasses both rain and drizzle events according to the definitions in *Zhou et al*. [2015]. The analysis was limited to samples in which the radar detected cloud top heights below 3 km, even though the frequency of occurrence of higher clouds is less than 4.1% per month during the period of study.

A narrow field-of-view (1.2°) Cimel Sun photometer was utilized to retrieve cloud optical thickness ($\tau$) and effective radius ($r_e$), with optimal operation during May, June, and the first two transects of July. Unlike Sun photometers in the Aerosol Robotic Network that operate in the normal aerosol mode for retrieving aerosol optical depth, the one deployed in MAGIC ran in cloud mode, that is, viewing zenith. The analysis method, described in *Chiu et al*. [2010, 2012], uses zenith radiances at wavelengths of 440, 870, and 1640 nm and

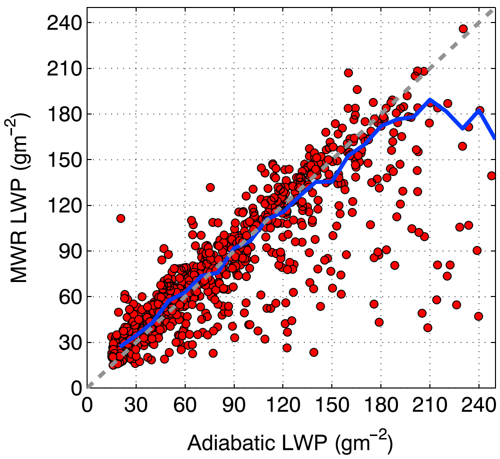


**Figure 1.** Ten-minute average MWR-determined LWP and adiabatic LWP for June and July of 2013. Blue line is the median MWR LWP as a function of its adiabatic counterpart with bin widths of 15 g/m$^2$. The gray dashed line denotes the 1:1 relationship.

retrieves $\tau$ and $r_e$ through minimizing the errors between the observed radiances and a lookup table constructed using a plane-parallel radiative transfer model for different values of $r_e$ and $\tau$. The actual instrument pointing angle was geometrically derived using the ship navigation data [*Chiu et al.*, 2016]. Assuming a cloud profile with a constant cloud droplet number concentration and linearly increasing effective radius with height, LWP can then be indirectly estimated as LWP $= \frac{5}{9}\rho_w r_e \cdot \tau$, with $\rho_w$ denoting the liquid water density. This assumption for the cloud vertical structure is supported by aircraft observations off the coast of California during the 2005 Marine Stratus/Stratocumulus Experiment (MASE) campaign [*Wang et al.*, 2009]. Since independent LWP retrievals are available from MWR during MAGIC, we will evaluate the water content stratification assumption by comparing MWR LWP with its adiabatic counterpart in section 3.

### 2.3. Satellite Cloud Retrievals

Standard satellite retrievals for MAGIC are described in P15 and briefly summarized here. Cloud property retrievals were derived from the GOES-15 imager and the MODIS on the Terra and Aqua satellites. Retrievals of $\tau$, $r_e$, cloud temperature, and cloud cover were produced using algorithms designed for MODIS for the Clouds and Earth's Radiant Energy System (CERES) project Edition 4 products [*Minnis et al.*, 2010, 2011] and adapted to GOES-15 [*Minnis et al.*, 2008]. Satellite LWP was computed as LWP $= \frac{5}{9}\rho_w r_e \cdot \tau$. While good agreement between aircraft observations and MODIS and GOES is reported in *Zheng et al.* [2011] and *Painemal et al.* [2012] for the southeast Pacific, we will further extend the comparison with the use of ship-based observations.

## 3. Adiabaticity and $N_d$ Calculation

One basic assumption in estimating both $N_d$ and LWP from visible/near-infrared ship and satellite-based retrievals is that the cloud liquid water content linearly increases with height. We tested this assumption by comparing the observed LWP (microwave) with its adiabatic counterpart (LWP$_{\mathrm{ad}}$). Following *Albrecht et al.* [1990], LWP$_{\mathrm{ad}}$ was calculated as

$$\mathrm{LWP}_{\mathrm{ad}} = \frac{\rho_a}{\rho_w} \Gamma_{\mathrm{ad}} \cdot \frac{\Delta Z^2}{2} \tag{1}$$

where $\rho_a$ and $\Gamma_{\mathrm{ad}}$ are the mean in-cloud air density and adiabatic lapse rate, respectively, and $\Delta Z$ is the cloud thickness. Equation (1) is obtained by vertically integrating the adiabatic liquid water content, which is in turn a linear function of height. Temperature and pressure profiles for $\rho_a$ and $\Gamma_{\mathrm{ad}}$ calculations were taken from radiosondes matched to the HSRL cloud base and radar cloud top height pair to within 4 h. A more restrictive temporal collocation criterion produced similar results but with a reduced number of matched samples. We selected the period June through July 2013, when all the active sensors were operational and radiosondes, needed for computing $\Gamma_{\mathrm{ad}}$, were launched frequently.

Figure 1 compares 10 min averaged MWR-determined LWP and LWP$_{\mathrm{ad}}$, from samples for boundary layer clouds only (top heights from the radar below 3 km) that are overcast (cloud frequency $> 0.95$) and have values between 15 and 250 g/m$^2$ and precipitation frequencies less than 0.1, to guarantee good quality MWR LWP. We note that at 15 g/m$^2$, the LWP has an associated error of around 30%, which is a substantial improvement over the uncertainties for two-channel microwave radiometer LWP retrievals [*Cadeddu et al.*, 2013]. The linear correlation of 0.85 with a small bias (11.8 g/m$^2$) suggests a near-adiabatic behavior. The 1:1 relationship between adiabatic and MWR LWP implies that the effect of cloud top entrainment is modest because the entrainment rate is small and/or the boundary layer turbulence is able to partially offset the

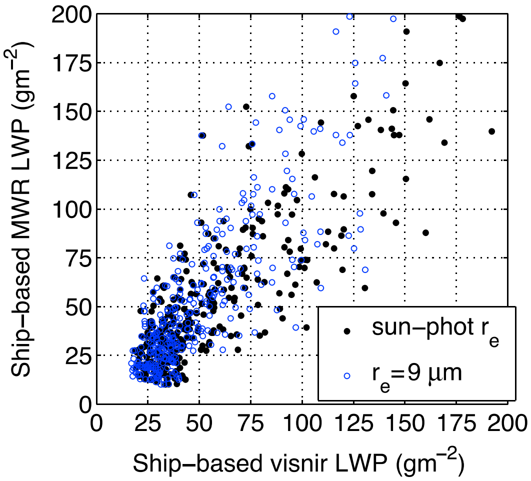


**Figure 2.** Ship-based comparison between Sun photometer (Sun-phot) LWP, derived from $r_e$ and $\tau$, and from MWR. Blue circles correspond to Sun photometer LWP derived from $\tau$ assuming a constant $r_e = 9$ μm.

cloud dilution. Mean LWP values of 83.3 and 94.87 g/m$^2$ from MWR and the adiabatic computation, respectively, are equivalent to a subadiabatic fraction, defined as the ratio of the MWR LWP to $LWP_{ad}$, of 0.88. This subadiabatic fraction is close to values reported by *Zuidema et al*. [2012] in the southeast Pacific using an airborne microwave radiometer, where median fractions ranged between 0.86 and 0.96. It is important to clarify that the adiabatic fraction is prone to uncertainties due to the combined errors in the radar and HSRL cloud boundary detections. For instance, we computed a Gaussian propagating error near 9.4 g/m$^2$ for the mean $LWP_{ad}$ caused solely by limitations in the instruments' vertical bin size resolution (7.5 and 30 m for the HSRL and radar, respectively).

$LWP_{ad}$ was also derived using the ceilometer cloud base height (not shown). This height averaged 47.5 m greater than that determined from the HSRL, even though the correlation between both estimates was high ($r = 0.99$). As a result, the ceilometer adiabatic calculations averaged 29.6 g/m$^2$ lower than those determined from the HSRL, implying an implausible cloud superadiabaticity. Given the HSRL's good calibration and its high sensitivity to water droplets, the HSRL cloud base height detection was used, as it was deemed more reliable.

### 3.1. Ship-Based Sun Photometer and Microwave Liquid Water Path Consistency

An advantage of the MAGIC campaign is that the availability of multi-instrument measurements allows testing of the physical consistency among different retrievals. Figure 2 (black dots) compares 10 min averaged LWP derived from the MWR and the Sun photometer (Sun-phot) LWP values for overcast samples with LWP less than 250 g/m$^2$. These retrievals have a positive linear correlation coefficient of 0.86 and a Sun-phot LWP positive bias of 6.7 g m$^{-2}$, although the relationship is rather scattered. Since Sun-phot LWP is a function of both $\tau$ and $r_e$, we isolate the effect of $\tau$ on LWP by simply assuming a constant $r_e$ at 9 μm, consistent with typical values found over the study region [e.g., *Lu et al*., 2007, Table 1], and recalculate the corresponding LWP. The comparison against MWR LWP (Figure 2, blue circles) shows a linear correlation coefficient of 0.82 and a Sun-phot LWP positive bias of 1.2 g m$^{-2}$, which are comparable to those obtained when using Sun-phot $r_e$. These results indicate that the good correlation between Sun-phot and MWR LWP is mainly due to Sun-phot $\tau$, with a small correlation improvement attributed to Sun-phot $r_e$. We note that retrieving $r_e$ from zenith radiance measurements is more challenging than retrieving $\tau$, because the competing processes between radiance reduction from stronger absorption for larger droplets and radiance enhancement due to stronger forward scattering weaken the sensitivity of zenith radiance to cloud droplet size, and makes it harder to improve the $r_e$ retrieval accuracy [*Chiu et al*., 2012]. Therefore, given the good agreement between the MWR LWP and Sun photometer $\tau$, they will be further applied to evaluate satellite observations, as well as for calculating $N_d$.

### 3.2. Consistency of Satellite and Ship-Based Cloud Retrievals

Before determining consistency between ship and satellite-based aerosol-cloud interaction (ACI) metrics, we compare ship and satellite retrievals of cloud properties. Following the methodology in P15, we spatially average the satellite data to a common 20 km resolution. This is intended to provide a more robust screening of partially cloudy scenes by utilizing only grids with cloud cover exceeding 95%. To be consistent with the satellite resolution, the ship-based data were hourly averaged (equivalent to a 20–40 km distance traveled by the ship). The LWP comparisons in Figure 3a and Table 2 show a linear correlation coefficient between MODIS (GOES-15) and the ship-based LWP data of 0.96 (0.88) with a mean bias of 12 g/m$^2$ (12.7 g/m$^2$). A similar, positive bias was also reported over the southeast Pacific by *Painemal and Zuidema* [2011] and

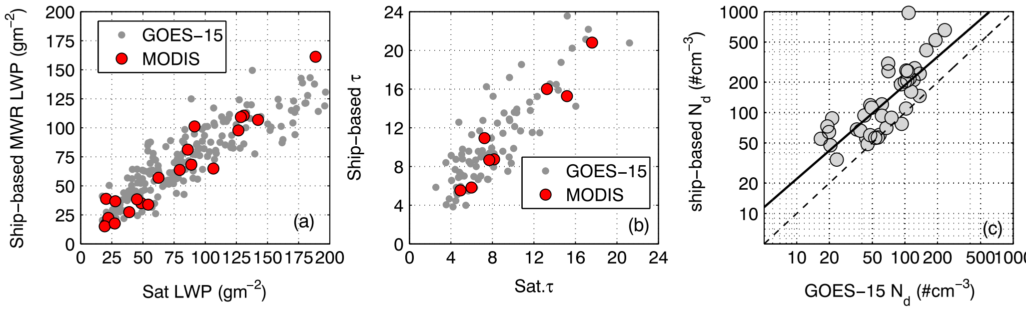


**Figure 3.** Scatterplot between GOES-15 (gray) and MODIS (red) satellite retrievals against their ship-based counterparts for (a) liquid water path (LWP) and (b) aerosol optical depth ($\tau$), and (c) GOES-15 cloud drop number concentration ($N_d$), with the solid line denoting the linear fit and the dashed line the 1:1 line.

*Painemal et al*. [2012]. Ship-based and satellite $\tau$ values are highly correlated (Figure 3b and Table 2), but with the satellite values negatively biased relative to the ship-based retrievals.

Given the near-adiabatic behavior of the clouds, we computed the ship-based $N_d$ using the relationship in *Painemal and Zuidema* [2013]:

$$N_d(\mathrm{LWP}, \tau)\ \left[\mathrm{cm}^3\right] = 0.058\left[\mathrm{g}^2\mathrm{cm}^{-6}\right]\cdot\frac{\Gamma_{\mathrm{obs}}{}^{1/2}}{k}\cdot\frac{\tau^3}{\mathrm{LWP}^{5/2}} \tag{2}$$

where $\Gamma_{\mathrm{obs}}$ is the observed stratification of the water content with height, and $k$ is the ratio between the cube of the effective radius and the mean volume radius of the droplet size distribution. The units for $\Gamma_{\mathrm{obs}}$ and LWP in equation (2) are in [g/cm$^4$] and [g/cm$^2$], respectively. Here we use a constant $\Gamma_{\mathrm{obs}} = 1.4$ g/m$^3$/km and $k = 0.88$, which are averaged values derived from aircraft data over the southeast Pacific during the VOCALS Regional Experiment [*Painemal and Zuidema*, 2011]. We reduce uncertainties in the retrievals due to thin clouds [e.g., *Lim et al*., 2016] by limiting the analysis to samples with LWP $> 15$ g/m$^2$.

Following a similar methodology, described in *Painemal and Zuidema* [2011], satellite $N_d$ is computed, assuming $r_e$ in [cm], as

$$N_d(r_e, \tau)\ \left[\mathrm{cm}^{-3}\right] = 1.41\times10^{-6}\left[\mathrm{cm}^{-1/2}\right]\cdot\frac{\tau^{1/2}}{r_e{}^{5/2}} \tag{3}$$

We apply equations (2) and (3) to the ship-based and satellite data, respectively, and compare ship-based and satellite $N_d$ in Table 2 and Figure 3c. The GOES-15 and the ship-based $N_d$ retrievals have a statistically significant (at 99% confidence level according to a Student's $t$ test) high correlation (with linear correlation coefficient 0.78), especially considering the rather dissimilar equations used to compute $N_d$. Their scatterplot in Figure 3c shows a linear relationship on a log-log scale, and although the ship-based $N_d$ tends to be larger than GOES-15, it is parallel to the 1-1 line (slope at 0.93), implying that these two quantities are only related by a constant factor. It is not possible to determine with the available measurements which $N_d$ values better resemble the real ones. Moreover, despite the magnitude differences between ship-based and satellite data, their values are reasonable and consistent with the range of variability observed during aircraft field campaigns off the coast of California [e.g., *Wang et al*., 2009]. The disagreement in terms of the absolute magnitude of $N_d$ appears to be associated with satellite $\tau$ underestimate relative to the Sun photometer retrieval. For instance, if one assumes that $\tau$ is the only source of uncertainty, and GOES $\tau$ is 20.7% smaller than its

**Table 2.** Linear Correlation Mean Bias and Root-Mean-Square Deviation Between MODIS (GOES-15) Retrieved Values and Ship-Based Observations[a]

| Quantity | Linear Correlation Coefficient $r$ | Mean Bias | Root-Mean-Square Deviation RMSD |
|---|---|---|---|
| LWP (g/m$^2$) | **0.96** (**0.88**) | 12, 13.4% (12.7, 16.8%) | 18.9 (26.4) |
| $\tau$ | **0.96** (**0.83**) | −1.46, −14% (−2.3, −20.7%) | 2.03 (3.26) |
| $N_d$ (cm$^{-3}$) | −0.29 (**0.78**) | −154.3, −61% (−101, −56%) | 261.3 (184.5) |

[a]Correlations in bold are statistically significant at 99% confidence level according to a Student's $t$ test.

ship-based counterpart (Table 2), it follows from equation (2) that GOES $N_d$ is 50% smaller than the ship-based $N_d$, a result consistent with the actual mean bias. Even though the linear correlation coefficient between ship-based and MODIS $N_d$ is small and negative (Table 2), the comparison is statistically insignificant because the statistics were calculated based on only six collocated samples.

### 3.3. Error Characterization

Since the intercomparison of several data sets and the ACI quantification entail the computation of slopes, we paid close attention to the calculation details. Instead of applying the standard least squares regression, we used the York fit regression [*York et al*., 2004]. This iterative method provides symmetrical slopes in $x$ and $y$ and is less affected by outliers than the standard linear regression [*Cantrell*, 2008]. For calculating York-derived slopes, measurement/retrieval errors need to be specified and are documented as follows.

For estimating satellite $N_d$ errors, we rely on comparisons over the southeast Pacific between 20 km averaged GOES-10 and aircraft microphysical observations. The root-mean-square error relative to the mean in *Painemal et al*. [2012] is approximately 30%, which is similar to the MODIS Gaussian error of 25% used in *Painemal and Zuidema* [2010]. For simplicity, we adopt a constant 30% error in $N_d$ for both the GOES-15 and MODIS retrievals.

We estimate the error in the ship-based $N_d$ by adopting a Gaussian propagation error methodology. This requires the uncertainty characterization of each term of equation (2). Sun photometer $\tau$ errors were estimated by adding randomly generated perturbations to the measurements during the retrieving process [*Chiu et al*., 2012]. This procedure yielded an averaged error of 19% in both $r_e$ and $\tau$ during MAGIC. Nevertheless, this value likely underestimates the overall error associated with the use of a 1-D radiative transfer (plane-parallel) model in the algorithm. An alternative error assessment was based on the comparison between synthetic cloud observations (from a large eddy simulation LES model with a horizontal resolution of 67 m) and plane-parallel cloud retrievals obtained from radiances simulated from the synthetic cloud scene [*Chiu et al*., 2012]. This comparison yielded a root-mean-square difference (RMSD) between the retrieved $\tau$ and that from the LES close to 30%. We utilize this error in our calculation because it better reflects the challenges of retrieving $\tau$ with the Sun photometer.

Additionally, we use a 15% error in the microwave LWP, which is the upper error reported in *Cadeddu et al*. [2013] associated with the mean LWP during MAGIC. For the parameter $k$ in equation (2), we use an uncertainty of 20%, a value that represents the spread of the $k$ distribution measured for the southeast Pacific stratocumulus clouds during VOCALS [*Painemal and Zuidema*, 2011]. The error in $\Gamma$ was estimated at 20%, which is slightly smaller than the standard deviation of the LWP subadiabatic fraction during MAGIC (30%), yet the contribution of $\Gamma$ to the overall error is modest. The combined $N_d$ Gaussian propagating error, calculated as the square root of the sum of the squared errors under the assumption that the individual errors are uncorrelated, is 100%, a value that can be substantially reduced by applying 10 min data averaging. This arbitrary temporal average allows enough samples in the averaging to reduce measurement errors while preserving part of the observational variance. Assuming 7 to 10 samples every 10 min (dictated by the availability of MWR data), the 10 min $N_d$ error becomes $100\%/\sqrt{7} = 38\%$. This error does not consider other sources of uncertainty such as the dissimilar instrument fields of view and the validity of equation (2). These factors appear to explain why previous studies that applied similar $N_d$ equations reported a high variability and at times very large $N_d$ values not observed in in situ aircraft data [e.g., *Lim et al*., 2016; *McComiskey et al*., 2009].

For aerosol properties, we also use the 10 min coefficient of variation as the fractional error. This yields mean errors of 11% for CCN concentration, 9% for UHSAS accumulation mode aerosol concentration (diameters between 0.1 and 1.0 μm), and 25% for the dry nephelometer measurements, after applying the corrections described in section 4.3.

## 4. Results

### 4.1. Satellite $N_d$ and Ship-Based CCN

ACI, defined as $ACI_{CCN} = \frac{\partial \ln(N_d)}{\partial \ln(CCN)}$ and derived from satellite $N_d$ and ship-based CCN, was examined in P15 for the full MAGIC deployment, with $ACI_{CCN}$ around 0.9 for linear fits of the logarithm of the GOES-15 $N_d$ versus

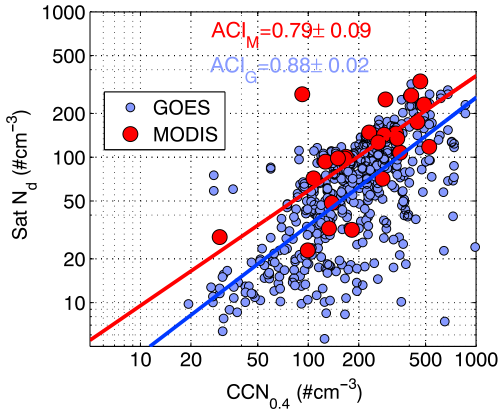


**Figure 4.** Scatterplot between $CCN_{0.4}$ and satellite $N_d$ for MODIS (red) and GOES (blue). $ACI_M$ and $ACI_G$ are the slopes for MODIS and GOES-15.

the logarithm of the CCN concentration at 0.4% supersaturation ($CCN_{0.4}$). Here we perform a similar analysis for the May–August 2013 sampling period (spring-summer). Figure 4 depicts the relationship between satellite $N_d$ from MODIS (red) and GOES-15 (blue) and $CCN_{0.4}$. The linear correlation coefficient of the logarithms of the two quantities is near 0.65 for both GOES-15 and MODIS. $ACI_{CCN}$ for each satellite cloud data set is $0.88 \pm 0.02$ for GOES ($ACI_G$) and $0.79 \pm 0.09$ for MODIS ($ACI_M$).

Even though satellite data offer a valuable alternative when other data sets are unavailable, the use of ship observations is more appropriate because they are spatially/temporally collocated with the CCN measurements, and the instruments sampled cloud structures that were much smaller than those observed by satellites.

### 4.2. Ship-Based Computation of Aerosol-Cloud Interactions

Figure 5a shows the relationship between 10 min averaged $CCN_{0.4}$ and $N_d$ using overcast samples, defined as those samples with ceilometer cloud frequency higher than 0.95 (gray circles), to reduce the effect of 3-D radiative effects near the cloud edges (at visible/near-infrared wavelengths) and clear-sky contamination in the retrievals. The red circles correspond to samples with precipitation occurrence frequency more than 10%. Additionally, the $CCN_{0.3}$-$N_d$ data for nonprecipitating samples are also depicted (blue open circles). The overall $CCN_{0.4}$-$N_d$ correlation is high and statistically significant ($r = 0.79$), and the slope of the logarithm of ship-based $N_d$ versus logarithm of $CCN_{0.4}$ ($ACI_{CCN}$) is $1.39 \pm 0.10$, with ±0.10 denoting the standard error of the slope. $ACI_{CCN}$ slightly decreases to $1.30 \pm 0.13$ when only nonprecipitating samples are considered. These values are slightly greater than the physical upper limit of 1.0, at which the fractional change in aerosol is linked to an equivalent fractional change in $N_d$. It is plausible that the calculations are not robust due to the small number of samples. This is mainly due to the CCN counter 10 min sampling cycle with constant supersaturation. We repeated the nonprecipitating ACI calculation but using $CCN_{0.3}$ instead and found a smaller value at $0.98 \pm 0.12$, which is within the expected physical values. It is unclear why both $CCN_{0.4}$ and $CCN_{0.3}$ do not yield the same ACI, especially when considering that both CCN measurements are strongly correlated at 0.98 with a logarithmic slope of 1.0. As previously mentioned, the small number of samples (Table 3), due to gaps in the radar data set, might be the reason for the ACI disagreement. When repeating the ACI calculation using all the available samples irrespective of the radar data availability, the number of points increases more than 35%, and the different CCN-based calculations start to converge, with ACI at 0.97 and 1.18 for $CCN_{0.3}$ and $CCN_{0.4}$, respectively. Similarly, the use of CCN at 0.2% ($CCN_{0.2}$) produces an $ACI = 1.11 \pm 0.14$. We did not report the $CCN_{0.2}$-based ACI for nonprecipitating scenes because the number of samples was small (less than 15) and the $CCN_{0.2}$-$N_d$ correlation was statistically insignificant.

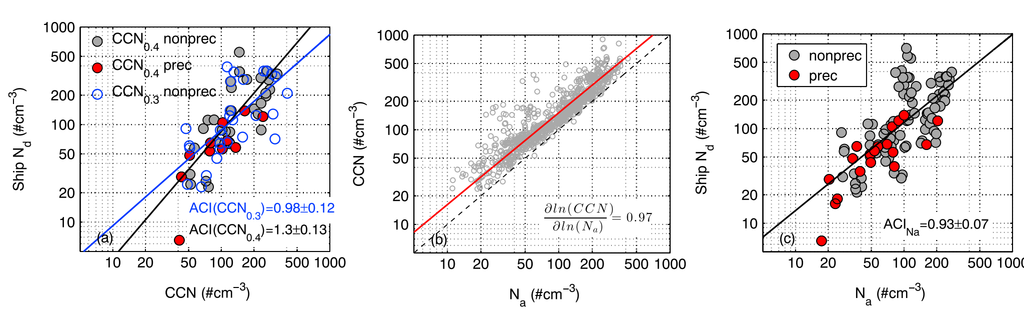


**Figure 5.** Ten-minute averaged relationships for (a) $N_d$ and $CCN_{0.4}$ (gray and red), and $CCN_{0.3}$ and $N_d$ (blue open circles, nonprecipitating samples) (b) $CCN_{0.4}$, and accumulation mode aerosol $N_a$, and (c) $N_d$ versus $N_a$. Red circles are samples with precipitation frequency of occurrence of more than 10%. ACI is reported for nonprecipitating samples only.

**Table 3.** ACI Determined Using 10 min Averaged Ship-Based $N_d$ and Different Aerosol Properties $\alpha$[a]

| Aerosol Property | $ACI_{CCN}$ | Correlation (Log Scale) | Number of Matched Samples |
|---|---|---|---|
| $CCN_{0.4}$ | 1.39 (1.3) | 0.79 (0.76) | 54 (36) |
| $CCN_{0.3}$ | 0.96 (0.98) | 0.65 (0.65) | 35 (28) |
| $N_a^{0.97}$ | 1.04 (0.95) | 0.72 (0.66) | 104 (85) |
| $\sigma_{ext}^{0.87}$ | 1.15 (1.1) | 0.73 (0.71) | 61 (48) |

[a]Parenthetical values correspond to statistics after removing samples with precipitation frequency >0.1. All correlations are statistically significant at 99% confidence level according to a Student's *t* test.

We further constrain the aerosol-cloud interaction metric by using the accumulation mode aerosol concentration ($N_a$, diameters between 100 nm and 1.0 μm) derived from the UHSAS and compute a $N_a$-based ACI as $ACI_{Na} = \frac{\partial \ln(N_d)}{\partial \ln(N_a)}$. The use of $N_a$ is reasonable as the fraction of aerosols activated into CCN is typically high for aerosol diameters larger than 100 nm and supersaturations higher than 0.2% [e.g., *Bougiatioti et al.*, 2011]. One major advantage of using $N_a$ is that the number of samples is double than that for CCN. As a consistency check, we show in Figure 5b the relationship between $N_a$ and $CCN_{0.4}$ for all-sky observations during both day and night. The correlation between both aerosol quantities is high ($r = 0.90$), and the slope of the logarithm of $CCN_{0.4}$ versus logarithm of $N_a$ is near 1.0 (0.97). When the $N_d$-CCN analysis of Figure 5a was repeated but used $N_a$ instead of CCN (Figure 5c), the correlation is high ($r = 0.72$) and $ACI_{Na}$ is also high at $1.00 \pm 0.05$, the physical upper limit. The nonprecipitating $ACI_{Na}$ values slightly decrease to $0.93 \pm 0.07$, mostly due to the effect of removing very low concentrations of $N_a$ and $N_d$. After using the slope in Figure 5b to infer $CCN_{0.4}$ from $N_a$, the equivalent $ACI_{CCN}$

$$ACI_{CCN} = \frac{\partial \ln(N_d)}{\partial \ln(N_a)} \cdot \frac{\partial \ln(N_a)}{\partial \ln(CCN)} = \frac{ACI_{Na}}{0.97} \tag{4}$$

becomes 1.03 and 0.96 for all and nonprecipitating samples, respectively.

We also repeated the previous analysis but used hourly averages to emulate the spatial resolution of the satellite. We compare $N_d$ against both $CCN_{0.4}$ and $N_a$ (Figure 6). As in Figure 5, the samples having more precipitation occurrences are associated with low concentrations of aerosols and $N_d$. The slopes are not different from their 10 min counterparts, and overall, their $ACI_{CCN}$ and $ACI_{Na}$ values are near 1.0. These slopes are only 10%–20% greater than those derived from satellite $N_d$ and ship-based $CCN_{0.4}$.

### 4.3. Aerosol Scattering ($\sigma_{scatt}$), Extinction Coefficient ($\sigma_{ext}$), and $N_d$ Slope

*Shinozuka et al.* [2015] evaluated the use of dry aerosol scattering ($\sigma_{scatt}$) and extinction ($\sigma_{ext}$) coefficients as proxies for CCN concentrations. In their study, CCN concentration is assumed to be directly proportional to $\sigma_{ext}^{\beta}$ with $\beta$ between 0.5 and 0.9, depending on the geographical region considered. We used this relationship with MAGIC data to compute $\beta$ and evaluate the use of $\sigma_{ext}$ in calculating the ACI metric. Aerosol hygroscopic growth can result in much larger diameters of particles and thus substantially alter the scattering properties.

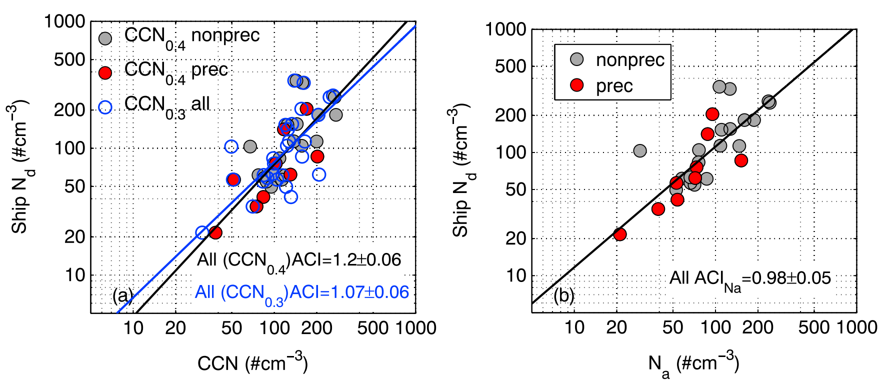


**Figure 6.** Hourly averaged relationship between (a) $CCN_{0.4}$ and $N_d$ (gray and red) and $CCN_{0.3}$ and $N_d$ (open blue circles), and (b) $N_a$ and $N_d$. Red circles are samples with precipitation frequency of occurrence of more than 10%.

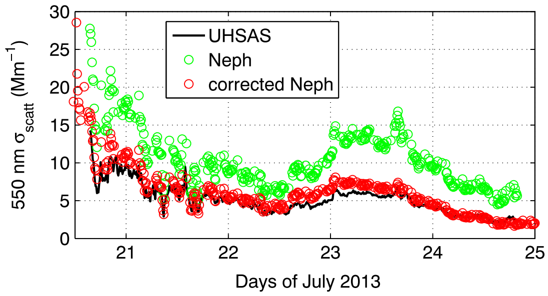


**Figure 7.** The 550 nm light scattering coefficient time series during a July leg (Leg 15A, California-Hawaii). Green circles denote raw nephelometer measurements. Red circles are the corrected nephelometer $\sigma_{dry}$ after applying the humidification factor correction. Solid black line is the Mie calculation derived using the UHSAS particle size distribution and refractive index at 1.53 + 0.0i, typical of ammonium sulfate.

Thus, before the analysis was performed, a simple correction method was devised to convert the observed measurements of aerosol scattering coefficient made at relative humidity (RH) values near 70%, $\sigma_{neph}$, to dry scattering coefficients, $\sigma_{dry}$, the quantity that can be more directly related to aerosol number concentration. The method relies on a simple parameterization that relates the humidified-to-dry scattering coefficient ratio, $\sigma_{neph}/\sigma_{dry}$, defined as a humidification factor *f*(RH), to RH using the expression reported by *Gasso et al.* [2000] over the northern Atlantic for a clean marine air mass:

$$f(\mathrm{RH}) = 0.76\cdot\left(1-\frac{\mathrm{RH}}{100}\right)^{-0.69} \quad (5)$$

The constant parameters in equation (5) can also be estimated with measurements of light scattering at low and high RH. Although a second nephelometer during MAGIC measured aerosol scattering at varying relative humidity, it did not perform as designed. With a very limited number of samples, we derived *f*(RH) when at least one instrument measured at RH <45% and we found a parameterization, $f(\mathrm{RH}) = 0.73\cdot\left(1-\frac{\mathrm{RH}}{100}\right)^{-0.63}$, which is similar to and partially confirms equation (5).

Even though it is not possible to fully evaluate how well equation (5) represents the conditions during MAGIC, we can test whether the corrected $\sigma_{dry}$ is consistent with Mie calculations for a specific aerosol species. For this purpose, we used dry aerosol size distributions obtained from the UHSAS and assumed a refractive index of ammonium sulfate at 1.53 + 0.0i [*Toon et al.*, 1976], a value similar to that for sodium chloride (two dominant aerosol species in the marine boundary layer). Given that UHSAS only derives distributions for particles with optical diameters less than 1 μm, we only used nephelometer observations when the instrument operated with a 1 μm cutoff.

Figure 7 shows the time series of scattering coefficients for a specific California-Hawaii transect. Green circles are the uncorrected nephelometer data at 550 nm, the corrected $\sigma_{dry}$ is in red, and the Mie-calculated $\sigma_{scatt}$ (based on UHSAS data) is in black. The agreement between $\sigma_{dry}$ and the Mie-calculated values is remarkable, lending support to the use of the simple humidification factor. The figure also shows the magnitude of changes due to RH. At times, nephelometer data are two times greater than the corrected $\sigma_{dry}$. The linear correlation coefficient of the Mie-calculated dry scattering coefficient and the uncorrected $\sigma_{scatt}$ is 0.86, while the bias is 2.87 (45%), with a RMSD of 4.95 M m$^{-1}$ (79% relative to the mean). In contrast, the corrected $\sigma_{scatt}$ ($\sigma_{dry}$) is on average only 0.39 Mm$^{-1}$ (11%) greater than the value of $\sigma_{scatt}$ calculated from the UHSAS, with a linear correlation coefficient of 0.91, and a RMSD of 1.44. Because of the good agreement between the corrected $\sigma_{dry}$ and $\sigma_{scatt}$, in the following analysis we will only make use of $\sigma_{dry}$.

Next, we compared 10 min averaged $\sigma_{dry}$ with $CCN_{0.4}$ for $\sigma_{dry}$ greater than 0.1 Mm$^{-1}$ to remove samples more affected by instrument noise. As in *Shinozuka et al.* [2015], the slope calculation between the logarithms of $\sigma_{dry}$ and CCN is justified by the high-correlation coefficient (0.8) in Figure 8a. We adopted a $\sigma_{dry}$ fractional error of 25% (coefficient of variation) for computing the York fit. This error is more than double that assumed by *Shinozuka et al.* [2015] and highlights the inherent challenges of ship deployments. We found a slope for the linear fit of the logarithms of $CCN_{0.4}$ and $\sigma_{dry}$ to be $\beta = 0.82 \pm 0.01$ or equivalent to $CCN_{0.4} \propto \sigma_{dry}^{0.82}$. Since the aerosol extinction coefficient ($\sigma_{ext}$) is the physical quantity that can be more closely related to other aerosol remote sensing measurements, we repeated the analysis depicted in Figure 8a but for $\sigma_{ext}$. We first computed $\sigma_{ext}$ by combining $\sigma_{dry}$ and dry aerosol absorption coefficient ($\sigma_{abs}$) measured by the PSAP and previously converted to 550 nm absorption (section 2). Figure 8b shows the CCN-$\sigma_{ext}$ relationship, which closely resembles that in Figure 8a, reflecting the weak aerosol absorption measured during MAGIC. The correlation of the logarithms of these two quantities is high ($r = 0.84$), and the slope slightly increases to $\beta = 0.87 \pm 0.01$ because, in logarithmic scale, inclusion of small $\sigma_{abs}$ tends to mainly affect the lower left region of the CCN-$\sigma_{ext}$

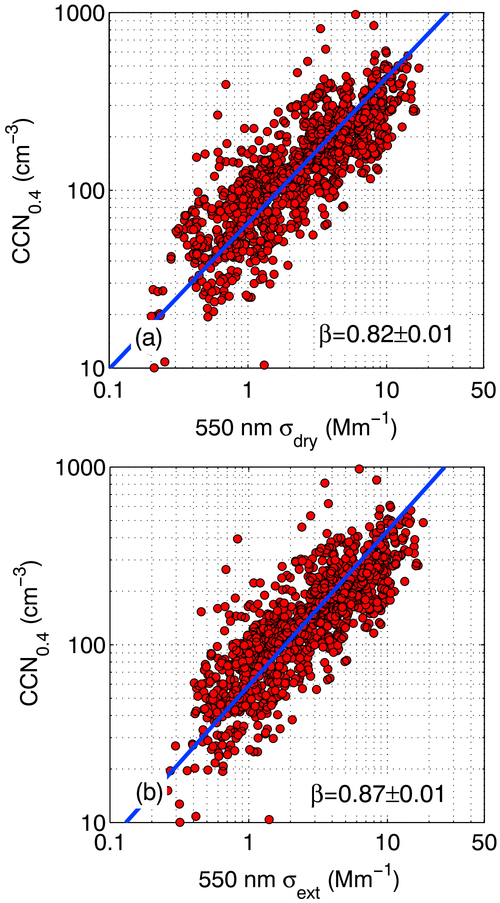


**Figure 8.** Scatterplot between $CCN_{0.4}$ and (a) dry aerosol scattering coefficient, and (b) extinction coefficient, $\beta$ denotes the logarithmic slope (blue).

scatterplot by shifting it to the right. This factor $\beta = 0.87$ is similar to that found for ground-based ARM observations over the Azores/Graciosa Island in *Shinozuka et al.* [2015] of 0.83 (weight averaged by frequency of occurrence). This agreement is likely due to the similarities of these two marine boundary layer regimes in terms of their aerosol composition.

Having a way to relate $\sigma_{ext}$ to CCN, we utilize $\sigma_{ext}$ to derive $ACI_{\sigma} = \frac{\partial \ln(N_d)}{\partial \ln(\sigma_{ext})}$. We first show in Figure 9 the $N_d$-$\sigma_{ext}$ relationship for 10 min averaged data. The logarithmic-scale linear correlation coefficient is 0.73 and the $\sigma_{ext}$-CCN slope ($ACI_{\sigma}$) is $1.00 \pm 0.07$ and $0.95 \pm 0.08$ for all and for precipitating samples, respectively. Using the exponent $\beta$, we can obtain the conversion from $ACI_{\sigma}$ to $ACI_{CCN}$ as $ACI_{CCN} = \frac{\partial \ln(N_d)}{\partial \ln(\sigma_{ext})} \cdot \frac{\partial \ln(\sigma_{ext})}{\partial \ln(CCN)} = \frac{ACI_{\sigma}}{\beta}$. This yields equivalent $ACI_{CCN}$ of 1.15 and 1.10 for all and nonprecipitating samples, respectively.

## 5. Discussion

### 5.1. Boundary Layer Deepening, Decoupling, and Aerosol Vertical Structure

Analysis of $ACI_{CCN}$ variability along the westward transects using GOES $N_d$ and ship-based CCN during the full MAGIC deployment in P15 showed that ACI values calculated from CCN concentration tend to decrease westward, as LWP decreases [*Painemal et al.*, 2016] and the boundary layer deepens and becomes less turbulently coupled. To confirm this finding, we computed $ACI_{Na}$ using nonprecipitating ship-based $N_d$ and $N_a$ for two groups with mean cloud base height less than and greater than the mean value of 835 m. In agreement with P15, it was found that the samples with shallower cloud bases (mean base at 577 m) have an overall linear correlation coefficient of 0.81 (logarithmic scale) and $ACI_{Na} = 1.09$ (equivalent to $ACI_{CCN} = 1.12$), whereas the correlation and $ACI_{Na}$ decreases to 0.43 and 0.58 (equivalent to $ACI_{CCN} = 0.60$), respectively, for the deeper subcloud layer group (mean base at 1207 m). On average, the shallow subcloud layer (high ACI) is also well coupled; the cloud base height and lifting condensation level difference is 146 m, 432 m less than that for the deeper layer. These findings lead us to hypothesize that the boundary layer depth and the level of turbulent coupling determine how representative aerosol surface measurements are of those expected near the cloud base, where CCN activation typically occurs.

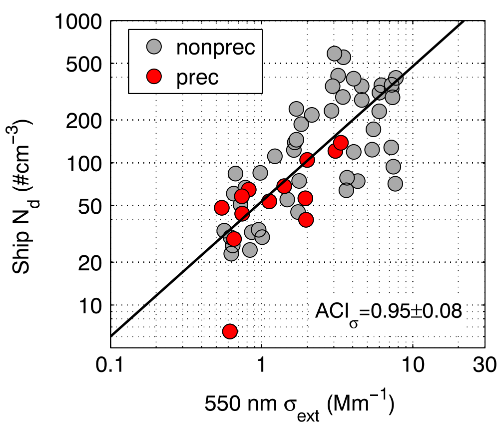


**Figure 9.** Scatterplot between 10 min averaged $N_d$ and 550 nm $\sigma_{ext}$. $ACI_{\sigma}$ is reported for nonprecipitating samples only.

To evaluate this hypothesis, we use vertically resolved HSRL measurements of particle backscatter cross section per unit volume ($\sigma_{back}$). Although in principle, HSRL can provide aerosol

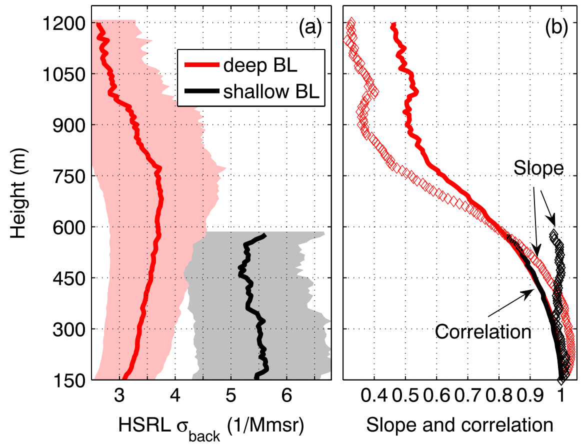


**Figure 10.** (a) Below-cloud particle backscatter cross section per unit volume ($\sigma_{back}$) from HSRL. Width of shaded area denotes half standard deviation. (b) Linear correlation (solid) and slope (diamonds) in logarithmic scale between 150 m backscatter ($\sigma_{back}$(150 m)) and levels above (solid lines). Red and black lines are statistics derived from samples with cloud base below and above 835 m (deep and shallow boundary layers, BL, respectively). The profiles extend up to the mean cloud base height.

extinction retrievals, these measurements are prone to several uncertainties (section 2). Given the relatively homogeneous $\sigma_{ext}$ to $\sigma_{back}$ ratio (lidar ratio) in marine environments [e.g., *Burton et al.*, 2012], $\sigma_{back}$ should capture the variability in $\sigma_{ext}$. In terms of near-surface observation, $\sigma_{ext}$, derived from the nephelometer and PSAP operated at the 10 μm cutoff diameter mode, is a measurement physically comparable to that retrieved from HSRL. Unfortunately, the nephelometer did not measure at the ambient relative humidity, and thus further corrections would be necessary to account for the disparity between instrument and ambient humidity. The adequacy of such a correction is not possible to test, for instance, with Mie calculations, because the UHSAS did not determine the aerosol size distribution, necessary for scattering computations, for diameters larger than 1 μm. We circumvent the limitations in the surface measurements by investigating the role of the aerosol vertical structure in the context of the HSRL $\sigma_{back}$. That is, the covariability in the subcloud layer backscatter cross section as a function of height $\sigma_{back}$ ($\sigma_{back}(z)$) is analyzed with respect to the lowest HSRL measurement at 150 m ($\sigma_{back}$(150 m)), which is in turn used as a surrogate for near-surface aerosol observation. We first show in Figure 10a the mean HSRL $\sigma_{back}(z)$ profiles for the shallow and deep boundary layers, previously defined as those samples with cloud bases lower and higher than 835 m, respectively. These profiles were created after removing HSRL retrievals above the cloud base. The mean $\sigma_{back}$ for the shallow composite (black) is greater than its deep composite counterpart (red) over the comparable height range, consistent with greater anthropogenic contributions near the coast, where the boundary layer is also shallower (P15). Next, we correlate $\sigma_{back}(z)$ with $\sigma_{back}$(150 m) and calculate its logarithmic slope, $\partial \ln(\sigma_{back}(150\ \mathrm{m}))/\partial \ln(\sigma_{back}(z))$, using an iteratively reweighted least squares fit with a bi-square weighting function to reduce the effect of outliers [*Street et al.*, 1988]. As expected, $\sigma_{back}(z)$ correlates well with $\sigma_{back}$(150 m) for both shallow and deep boundary layers at elevations below 450 m, with values of the linear correlation coefficient greater than 0.9 (Figure 10b, solid black and red, respectively). The relationship becomes more scattered, and the correlation decreases to below 0.5 for heights above 900 m, near the cloud base in the deep boundary layer case. On the other hand, the slope is near unity below 400 m for both groups (diamonds), although for the shallow-layer case, values near unity are observed throughout the subcloud layer. In contrast, the slope starts to decrease in the deep boundary layer above 450 m, reaching a minimum near 0.4 at 900 m. These findings demonstrate that in deep boundary layers, the use of surface aerosol observations would tend to yield ACI indices and correlation coefficients less than those calculated using near cloud base aerosol measurements.

### 5.2. Ship-Based ACI Calculations

One limitation of this study is the use of $N_d$ computed under the assumption of a near-adiabatic cloud model. We partially validated this assumption by showing a strong linearity between adiabatic and measured LWP. On the other hand, since we are mostly interested in the slope of $N_d$ with respect to a given aerosol property rather than $N_d$ absolute values, we argue that these slopes reduce the impact of $N_d$ uncertainties and assumptions about the cloud microphysical structure, whereas the strong linear correlations support the computation of slopes. A second aspect is that we did not stratify our calculation as a function of LWP as in previous studies [e.g., *Painemal and Zuidema*, 2013; *McComiskey and Feingold*, 2012]. Although accounting for LWP is essential for radiative transfer computations of the indirect effect, $N_d$ is weakly correlated with LWP ($r = -0.2$) and at least from the $N_d$-aerosol slope calculation viewpoint, LWP stratification is unnecessary.

**Table 4.** $ACI_{CCN}$ Determined Using Hourly Averaged Ship-Based and Satellite $N_d$ Combined With Different Aerosol Measurements $\alpha$[a]

| $N_d$-$\alpha$ | $ACI_{CCN}$ | Correlation (Log Scale) | Number of Matched Samples |
|---|---|---|---|
| Hourly $N_d$-$CCN_{0.4}$ | 1.2 | 0.77 | 29 |
| Hourly $N_d$-$CCN_{0.3}$ | 1.07 | 0.67 | 28 |
| Hourly $N_d$-$N_a^{0.97}$ | 1.01 | 0.78 | 29 |
| MODIS $N_d$-$CCN_{0.4}$ ($N_a^{0.97}$) | 0.79 (0.97) | 0.65 (0.69) | 24 (31) |
| GOES-15 $N_d$-$CCN_{0.4}$($N_a^{0.97}$) | 0.88 (0.92) | 0.66 (0.71) | 534/(626) |

[a]Parenthetical values were estimated by combining satellite $N_d$ and $N_a^{0.97}$. All correlations are statistically significant at 99% confidence level according to a Student's *t* test.

The 10 min average ACI calculations using CCN, $N_a$, and $\sigma_{ext}$ (after applying the regressions) are summarized in Table 3. As previously mentioned, all the aerosol observations yield $ACI_{CCN}$ near 1.0, although $CCN_{0.4}$ and $CCN_{0.3}$ yield slightly greater values. Given the anthropogenic contribution from particles with diameters less than 70 nm in the CCN measurements during MAGIC, along with the reduced number of collocated samples, the CCN-based ACI calculation might be less robust. On the other hand, $N_a^{0.97}$ and $\sigma_{ext}^{0.85}$ produce very similar $ACI_{CCN}$ values, because particle sizes larger than 100–200 nm typically dominated the light scattering during MAGIC [*Seinfeld and Pandis*, 2006].

The ship-based results in this study are comparable to those derived over the Southeast Pacific during the 2008 VOCALS Regional Experiment, where ACI values derived from in situ microphysical airborne probes ranged between 0.71 and 0.92, [*Painemal and Zuidema*, 2013; *Zheng et al*., 2011]. *McComiskey and Feingold* [2008] reported an ACI = 0.85 using measurements in *Twohy et al*. [2005] during the DYCOMS-II (Dynamics and Chemistry of Marine Stratocumulus-II) campaign over the northeast Pacific. In addition, averaged flight data during MASE reported by *Daum et al*. [2007, Figure 14a] yield and ACI ≈ 1.07. Overall, aircraft studies over the eastern Pacific yield an ACI range of 0.71–1.07, which is in close agreement with ACI values calculated from MAGIC data.

### 5.3. Satellite and Ship-Based Observations

The observational disagreement between aerosol-cloud interaction calculations derived from different data sets has been in part associated with the dissimilar spatiotemporal scales inherent in each platform [e.g., *McComiskey and Feingold*, 2012]. Since data averaging leads to variance reduction, it has been hypothesized that the large satellite fields of view explain in part the lesser satellite ACI values and weaker correlations between satellite retrievals of aerosols and cloud microphysics. Nevertheless, our analysis shows that an $ACI_{CCN}$ value of 0.88–0.92, based on combined satellite $N_d$ and ship-based CCN and $N_a$, is only slightly less than the hourly averaged ship-based $ACI_{CCN}$ of ~1.01–1.2 (Table 4). Moreover, ship-based 10 min and hourly calculations also agree well. These results suggest that for the overcast clouds having little precipitation reported in this study, the spatial variability is small, and thus satellite data yield results comparable to those from in situ observations. Based on these results, we speculate that an important and partially ignored source of disagreement between satellite-based and in situ calculations is the use of satellite aerosol optical depth (AOD) as a CCN concentration proxy. AOD is problematic, as it is a vertically integrated quantity and may not fully represent the aerosol variability in the boundary layer. A second issue is that a few large particles can dominate AOD while contributing little to CCN concentration. In addition, several artifacts can modulate the AOD-cloud covariability, having the potential to produce a spurious aerosol-cloud interaction signal (see discussion in P15). Even if AOD is used as a substitute for CCN, the nonlinear relationship $CCN \propto \tau_A^{\varepsilon}$, with $\varepsilon < 1$, [e.g., *Andreae*, 2009] would imply $\frac{\partial \ln(N_d)}{\partial \ln(\mathrm{AOD})} < \frac{\partial \ln(N_d)}{\partial \ln(\mathrm{CCN})}$

## 6. Conclusions

The MAGIC deployment provided an unprecedented data set of aerosol and cloud properties over the northeast Pacific boundary layer. We used remotely sensed MAGIC retrievals of cloud properties to compute $N_d$ and quantify its covariability with CCN and aerosol concentrations. We found that the value of an aerosol-cloud interaction index defined by $ACI_{CCN} = \partial \ln(N_d)/\partial \ln(\alpha)$), with $\alpha$ denoting CCN concentration, $N_a$, or $\sigma_{ext}$, is high and is near the upper physical limit of 1.0. The results are robust, whether using either 10 min or hourly averaged data. In addition, a reduction of up to 10% in ACI after removing precipitating samples is associated with the effect of filtering low CCN concentration and $N_d$ in the regression computation. The high ACI and correlations derived here exceed those from a similar ARM deployment at Point Reyes on the California coast [*McComiskey et al*., 2009], while the MAGIC $N_d$ is smaller and more physical than those reported in *Lim et al*. [2016]. Unlike the aforementioned studies, the use of a narrow field-of-view Sun photometer and improved LWP retrievals from a three-channel MWR is likely the main reason for the aerosol-cloud consistency reported here [*Lim et al*., 2016].

A remarkable finding is the agreement between ACI values derived using the satellite $N_d$ and that determined from only ship-based values. While this result was prefigured in the good agreement between satellite and ship-based cloud retrievals, it is surprising that despite the different spatial samplings and retrieval algorithms, the satellite cloud microphysics reproduce the ship-based ACI, which is in turn consistent with aircraft measurements taken in other marine boundary layer regimes. This result is encouraging and provides evidence that in overcast scenes with favorable satellite viewing angles, satellite cloud products provide valuable microphysical information, especially when in situ data set is unavailable.

We note that due to the limitations of MAGIC ship-based deployments, this study is primarily based on the relationship between $N_d$ and CCN for fixed values of supersaturation. A more rigorous study should account for the updraft magnitude and the associated supersaturation for each sampling for a better ACI quantification. Since we are only utilizing overcast samples with LWP greater than 15 g/m$^2$ (section 3), it is likely that the analysis is inadvertently biased toward measurements with stronger updrafts and supersaturations, for which $CCN_{03}$ and $CCN_{0.4}$ might be representative of the activated aerosols. Other factors unaccounted for in our study are the role of the cloud top entrainment in modifying $N_d$, precipitation, and the cloud vertical structure, especially when this departs from the assumptions that allow for $N_d$ calculations using equations (2) and (3).

The use of vertically resolved aerosol properties from a HSRL opens new opportunities for the investigation of the aerosol indirect effect, in principle, enabling better estimates than those based on surface observations only, which suffer from limitations in deep and decoupled marine boundary layers. *Ghan and Collins* [2004] and *Ghan et al*. [2006] devised a method to derive CCN profiles using the relationship between surface CCN and lidar backscatter cross section, combined with knowledge of the humidification factor. Our analysis supports the applicability of the *Ghan and Collins* method for surface-based aerosol extinction. To further extend the method for use with HSRL, it would be desirable to have accurate aerosol extinction retrievals, vertical profiles of CCN, relative humidity, and information about the aerosol species that can be used to select a proper humidification factor to help account for aerosol hygroscopic growth in the HSRL measurements.

**Acknowledgments**

This work was supported by the U.S. Department of Energy (DOE), Office of Science, Office of Biological and Environmental Research (OBER): DOE-BER Atmospheric Science Research Program (ASR) grants DE-FOA-0000885 (D. Painemal, P. Minnis, and C. Yost) and DE-SC0011666 (J.C. Chiu), Atmospheric Radiation Measurement Infrastructure Basic Energy Sciences, under contract DE-AC02-06CH11357 (M. Cadeddu), and DOE-BER under contract DE-SC00112704 (E.R. Lewis). C. Yost was also supported by the NASA CERES program. The MAGIC data set was downloaded from the ARM archive available at http://www.archive. arm.gov/. MODIS and GOES-15 retrievals are available at http://www-pm. larc.nasa.gov or upon request. We thank Horizon Lines and the Captain and crew of the Horizon *Spirit* for their support and hospitality during MAGIC. The constructive comments and suggestions provided by three anonymous reviewers are greatly appreciated.

## References

Albrecht, B., C. Fairall, D. Thomson, and A. White (1990), Surface-based remote sensing of the observed and the adiabatic liquid water content of stratocumulus clouds, *Geophys. Res. Lett.*, *17*, 89–92, doi:10.1029/GL017i001p00089.

Anderson, T. L., et al. (1996), Performance characteristics of a high-sensitivity, three-wavelength total scatter/backscatter nephelometer, *J. Atmos. Oceanic Technol.*, *13*, 967–986.

Andreae, M. O. (2009), Correlation between cloud condensation nuclei concentration and aerosol optical thickness in remote and polluted regions, *Atmos. Chem. Phys.*, *9*, 543–556, doi:10.5194/acp-9-543-2009.

Bond, T. C., T. L. Anderson, and D. Campbell (1999), Calibration and intercomparison of filter-based measurements of visible light absorption by aerosols, *Aerosol Sci. Technol.*, *3*(6), 582–600, doi:10.1080/027868299304435.

Bougiatioti, A., A. Nenes, C. Fountoukis, N. Kalivitis, S. N. Pandis, and N. Mihalopoulos (2011), Size-resolved CCN distributions and activation kinetics of aged continental and marine aerosol, *Atmos. Chem. Phys.*, *11*, 8791–8808, doi:10.5194/acp-11-8791-2011.

Burton, S. P., R. A. Ferrare, C. A. Hostetler, J. W. Hair, R. R. Rogers, M. D. Obland, C. F. Butler, A. L. Cook, D. B. Harper, and K. D. Froyd (2012), Aerosol classification using airborne High Spectral Resolution Lidar measurements—Methodology and examples, *Atmos. Meas. Tech.*, *5*, 73–98, doi:10.5194/amt-5-73-2012.

Cadeddu, M. P., J. C. Liljegren, and D. D. Turner (2013), The Atmospheric radiation measurement (ARM) program network of microwave radiometers: Instrumentation, data, and retrievals, *Atmos. Meas. Tech.*, *6*, 2359–2372, doi:10.5194/amt-6-2359-2013.

Cai, Y., D. Montague, W. Mooiweer-Bryan, and T. Deshler (2008), Performance characteristics of the ultra-high-sensitivity aerosol spectrometer for particles between 55 and 800 nm: Laboratory and field studies, *J. Aerosol Sci.*, *39*(9), 759–769, doi:10.1016/j.jaerosci.2008.04.007.

Cantrell, C. A. (2008), Technical note: Review of methods for linear least-squares fitting of data and application to atmospheric chemistry problems, *Atmos. Chem. Phys.*, *8*, 5477–5487.

Carslaw, K. S., et al. (2013), Large contribution of natural aerosols to uncertainty in indirect forcing, *Nature*, *503*, 67–71.

Chiu, J. C., C.-H. Huang, A. Marshak, I. Slutsker, D. M. Giles, B. N. Holben, Y. Knyazikhin, and W. J. Wiscombe (2010), Cloud optical depth retrievals from the Aerosol Robotic Network (AERONET) cloud mode observations, *J. Geophys. Res.*, *115*, D14202, doi:10.1029/2009JD013121.

Chiu, J. C., A. Marshak, C.-H. Huang, T. Várnai, R. J. Hogan, D. M. Giles, B. N. Holben, E. J. O'Connor, Y. Knyazikhin, and W. J. Wiscombe (2012), Cloud droplet size and liquid water path retrievals from zenith radiance measurements: Examples from the atmospheric radiation measurement program and the aerosol robotic network, *Atmos. Chem. Phys.*, *12*, 10,313–10,329, doi:10.5194/acp-12-10313-2012.

Chiu, J.-Y. C., L. Gregory, R. Wagener (2016), *MAGIC Cloud Properties From Zenith Radiance Data Final Campaign Summary*, United States: DOE ARM Clim. Res. Facility, Pacific Northwest Natl. Lab., Richland, Washington, doi:10.2172/1242830.

Daum, P., Y. Liu, R. McGraw, Y. Lee, J. Wang, G. Senum, and M. Miller (2007), *Microphysical Properties of Stratus/Stratocumulus Clouds During the 2005 Marine Stratus/Stratocumulus Experiment (MASE)*, *Rep. BNL-77935-2007-JA*, Brookhaven Natl. Lab., Upton, New York.

Eloranta, E. W. (2005), High spectral resolution lidar, in *Lidar: Range-Resolved Optical Remote Sensing of the Atmosphere*, *Springer Ser. in Opt. Sci.*, edited by K. Weitkamp, pp. 143–163, Springer, New York.

Fielding, M. D., J. C. Chiu, R. J. Hogan, G. Feingold, E. Eloranta, E. J. O'Connor, and M. P. Cadeddu (2015), Joint retrievals of cloud and drizzle in marine boundary layer clouds using ground-based radar, lidar and zenith radiances, *Atmos. Meas. Tech.*, *8*, 2663–2683, doi:10.5194/amt-8-2663-2015.

Gasso, S., et al. (2000), Influence of humidity on the aerosol scattering coefficient and its effect on the upwelling radiance during ACE-2, *Tellus Ser. B*, *52*, 546–567.

Ghan, S. J., and D. R. Collins (2004), Use of in situ data to test a Raman lidar-based cloud condensation nuclei remote sensing method, *J. Atmos. Oceanic Technol.*, *21*, 387–394.

Ghan, S. J., et al. (2006), Use of in situ cloud condensation nuclei, extinction, and aerosol size distribution measurements to test a method for retrieving cloud condensation nuclei profiles from surface measurements, *J. Geophys. Res.*, *111*, D05S10, doi:10.1029/2004JD005752.

Hegg, D. A., D. S. Covert, H. H. Jonsson, and R. K. Woods (2012), A simple relationship between cloud drop number concentration and precursor aerosol concentration for the regions of Earth's large marine stratocumulus decks, *Atmos. Chem. Phys.*, *12*, 1229–1238, doi:10.5194/acp-12-1229-2012.

Hildebrand, P. H., and R. Sekhon (1974), Objective determination of the noise level in Doppler spectra, *J. Appl. Meteorol.*, *13*, 808–811, doi:10.1175/1520-0450(1974)013<0808:ODOTNL>2.0.CO;2.

Hudson, J. G., S. Noble, and V. Jha (2010), Stratus cloud supersaturations, *Geophys. Res. Lett.*, *37*, L21813, doi:10.1029/2010GL045197.

Kollias, P. E. E., et al. (2016), Development and applications of ARM millimeter-wavelength cloud radars, *Meteorol. Monogr.*, *57*, 17.1–17.19, doi:10.1175/AMSMONOGRAPHS-D-15-0037.1.

Lewis, E. R., and J. Teixeira (2015), Dispelling clouds of uncertainty, *Eos Trans. AGU*, *96*, doi:10.1029/2015EO031303.

Lim, K.-S. S., L. Riihimaki, J. M. Comstock, B. Schmid, C. Sivaraman, Y. Shi, and G. M. McFarquhar (2016), Evaluation of long-term surface-retrieved cloud droplet number concentration with in situ aircraft observations, *J. Geophys. Res. Atmos.*, *121*, 2318–2331, doi:10.1002/2015JD024082.

Lu, M.-L., W. C. Conant, H. H. Jonsson, V. Varutbangkul, R. C. Flagan, and J. H. Seinfeld (2007), The Marine Stratus/Stratocumulus Experiment (MASE): Aerosol-cloud relationships in marine stratocumulus, *J. Geophys. Res.*, *112*, D10209, doi:10.1029/2006JD007985.

McComiskey, A., and G. Feingold (2008), Quantifying error in the radiative forcing of the first aerosol indirect effect, *Geophys. Res. Lett.*, *35*, L02810, doi:10.1029/2007GL032667.

McComiskey, A., and G. Feingold (2012), The scale problem in quantifying aerosol indirect effects, *Atmos. Chem. Phys.*, *12*, 1031–1049, doi:10.5194/acp-12-1031-2012.

McComiskey, A., G. Feingold, A. S. Frisch, D. D. Turner, M. A. Miller, J. C. Chiu, Q. Min, and J. A. Ogren (2009), An assessment of aerosol-cloud interactions in marine stratus clouds based on surface remote sensing, *J. Geophys. Res.*, *114*, D09203, doi:10.1029/2008JD011006.

Miller, M. A., K. Nitschke, T. P. Ackerman, W. R. Ferrell, N. Hickmon, and M. Ivey (2016), The ARM mobile facilities, *Meteorol. Monogr.*, *57*, 9.1–9.15.

Minnis, P., et al. (2008), Near-real time cloud retrievals from operational and research meteorological satellites, *Proc. SPIE Int. Soc. Opt. Eng.*, *7107*, 710703, doi:10.1117/12.800344.

Minnis, P., et al, (2010), CERES Edition 3 cloud retrievals, AMS 13th Conf. Atmos. Rad., Portland, OR, June 27 – July 2, 5.4, 7 pp.

Minnis, P., et al. (2011), CERES Edition-2 cloud property retrievals using TRMM VIRS and Terra and Aqua MODIS data. Part I: Algorithms, *IEEE Trans. Geosci. Remote Sens.*, *49*(11), 4374–4400, doi:10.1109/TGRS.2011.2144601.

Painemal, D., and P. Zuidema (2010), Microphysical variability in southeast Pacific Stratocumulus clouds: Synoptic conditions and radiative response, *Atmos. Chem. Phys.*, *10*, 6255–6269, doi:10.5194/acp-10-6255-2010.

Painemal, D., and P. Zuidema (2011), Assessment of MODIS cloud effective radius and optical thickness retrievals over the southeast Pacific with VOCALS-REx in situ measurements, *J. Geophys. Res.*, *116*, D24206, doi:10.1029/2011JD016155.

Painemal, D., and P. Zuidema (2013), The first aerosol indirect effect quantified through airborne remote sensing during VOCALS-REx, *Atmos. Chem. Phys.*, *13*, 917–931.

Painemal, D., P. Minnis, J. K. Ayers, and L. O'Neill (2012), GOES-10 microphysical retrievals in marine warm clouds: Multi-instrument validation and daytime cycle over the southeast Pacific, *J. Geophys. Res.*, *117*, D19212, doi:10.1029/2012JD017822.

Painemal, D., P. Minnis, and M. Nordeen (2015), Aerosol variability, synoptic-scale processes, and their link to the cloud microphysics over the northeast Pacific during MAGIC, *J. Geophys. Res. Atmos.*, *120*, 5122–5139, doi:10.1002/2015JD023175.

Painemal, D., T. Greenwald, M. Cadeddu, and P. Minnis (2016), First extended validation of satellite microwave liquid water path with ship-based observations of marine low clouds, *Geophys. Res. Lett.*, *43*, 6563–6570, doi:10.1002/2016GL069061.

Quaas, J., et al. (2009), Aerosol indirect effects—General circulation model intercomparison and evaluation with satellite data, *Atmos. Chem. Phys.*, *9*, 8697–8717, doi:10.5194/acp-9-8697-2009.

Roberts, G. C., and A. Nenes (2005), A continuous-flow streamwise thermal-gradient CCN chamber for atmospheric measurements, *Aerosol Sci. Technol.*, *39*(3), 206–221, doi:10.1080/027868290913988.

Rosenfeld, D., S. Sherwood, R. Wood, and L. Donner (2014), Climate effects of aerosol-cloud interactions, *Science*, *343*(6169), 379–380, doi:10.1126/science.1247490.

Seinfeld, J., and S. Pandis (2006), *Atmospheric Chemistry and Physics: From Air Pollution to Climate Change*, pp. 450, Wiley, N. J.

Shinozuka, Y., et al. (2015), The relationship between cloud condensation nuclei (CCN) concentration and light extinction of dried particles: Indications of underlying aerosol processes and implications for satellite-based CCN estimates, *Atmos. Chem. Phys.*, *15*, 7585–7604, doi:10.5194/acp-15-7585-2015.

Street, J. O., R. J. Carroll, and D. Ruppert (1988), A note on computing robust regression estimates via iteratively reweighted least squares, *Am. Stat.*, *42*, 152–154, doi:10.2307/2684491.

Toon, O. B., J. B. Pollack, and B. N. Khare (1976), The optical constants of several atmospheric aerosol species: Ammonium sulfate, aluminum oxide, and sodium chloride, *J. Geophys. Res.*, *81*, 5733–5748, doi:10.1029/JC081i033p05733.

Twohy, C. H., M. D. Petters, J. R. Snider, B. Stevens, W. Tahnk, M. Wetzel, L. Russell, and F. Burnet (2005), Evaluation of the aerosol indirect effect in marine stratocumulus clouds: Droplet number, size, liquid water path, and radiative impact, *J. Geophys. Res.*, *110*, D08203, doi:10.1029/2004JD005116.

Wang, J., P. H. Daum, S. S. Yum, Y. Liu, G. I. Senum, M.-L. Lu, J. H. Seinfeld, and H. Jonsson (2009), Observations of marine stratocumulus microphysics and implications for processes controlling droplet spectra: Results from the Marine Stratus/Stratocumulus Experiment, *J. Geophys. Res.*, *114*, D18210, doi:10.1029/2008JD011035.

York, D., N. Evensen, M. L. Martinex, and J. D. B. Delgado (2004), Unified equations for the slope, intercept, and standard errors of the best straight line, *Am. J. Phys.*, *72*, 367–375.

Zheng, X., et al. (2011), Observations of the boundary layer, cloud, and aerosol variability in the southeast Pacific near-coastal marine stratocumulus during VOCALS-REx, *Atmos. Chem. Phys.*, *11*, 9943–9959, doi:10.5194/acp-11-9943-2011.

Zhou, X., P. Kollias, and E. Lewis (2015), Clouds, precipitation and marine boundary layer structure during MAGIC, *J. Clim.*, doi:10.1175/JCLI-D-14-00320.1.

Zuidema, P., D. Leon, A. Pazmany, and M. Cadeddu (2012), Aircraft millimeter-wave passive sensing of cloud liquid water and water vapor during VOCALS-REx, *Atmos. Chem. Phys.*, *12*, 355–369, doi:10.5194/acp-12-355-2012.